Title **First assessment of non-X-ray background in Line Emission Mapper (LEM) focal plane detector.**

Prepared by: S. Lotti Date : 27/01/2023

Inputs by: C. Kilbourne Date :

Checked by: C. Macculi, L. Piro Date :

Agreed by: Date :

Authorized by: Date :

DISTRIBUTION LIST

DOCUMENT CHANGE RECORD

Issue	Date	Changed Section	Description of Change
1	20/01/2023		1st Issue

Abbreviations and acronyms

Item	Meaning
AIT	Assembly Integration and Test
ASI	Agenzia Spaziale Italiana
ASW	Application Software
CADM	Configuration and Data Management
CNR	Consiglio Nazionale delle Ricerche
CPO	Central Project Office
CryoAC	Cryogenic Anticoincidence
FA	Funding Agency
FEE	Front End Electronics
FPA	Focal Plane Assembly
GSE	Ground Segment
ICU	Instrument Control Unit
INAF	Istituto Nazionale di Astrofisica
LEM	Line Emission Mapper
LPO	Local Project Office
MP	Management Plan
OBS	Organization Breakdown Structure
PA	Product Assurance
PBS	Product Breakdown Structure
PS	Project Scientist
SM	System Manager
UniGE	University of Genova
UniPA	University of Palermo

Item	Meaning
WBEE	Warm Back End Electronics
WBS	Work Breakdown Structure
WEE	Warm Electronics
X-IFU	X-ray Integral Field Unit

Applicable Documents

[AD#]	Doc. Reference	Issue	Title
[AD1]			

Reference Documents

[RD#]	Doc. Reference	Issue	Title
[RD1]	http://geant4.web.cern.ch/		Geant4: a simulation toolkit
[RD2]	AREMBES Geant4		AREMBES WP 7: Normalization of an isotropic flux in space in Geant4 simulations
[RD3]	TN_INAF_GCR_2018_001		GCR flux assessment for the ATHENA X-IFU particle background evaluation
[RD4]	https://doi.org/10.1002/2016JA022920		Empirical model of long-time variations of galactic cosmic ray particle fluxes
[RD5]	Exp Astron (2012) 33:39–53 DOI 10.1007/s10686-011-9269-7		The radiation environment in L-2 orbit: implications on the non-X-ray background of the eROSITA pn-CCD cameras
[RD6]	Arembes TN 4.1		Arembes TN 4.1: Software Implementation of Radiation Transport and Effects Models
[RD7]	Technical report RI OAS/2/2018		ATHENA/X-IFU Geant4 simulation: cut-off optimization
[RD8]	Exp Astron (2017): DOI 10.1007/s10686-017-9538-1		The particle background of the X-IFU instrument
[RD9]	TN_INAF_GCR_2018_001	1	GCR flux assessment for the ATHENA X-IFU particle background evaluation
[RD10]	TN_INAF_HTM_2018_001	1	Validation of the HITOMI SXS particle background by Geant4

[RD#]	Doc. Reference	Issue	Title
[RD11]	XIFU-INAF-BKG-TN-0002		Assessment of non-X-ray background in the X-IFU.
[RD12]	NIST ESTAR references		https://physics.nist.gov/PhysRefData/Star/Text/ref.html
[RD13]	EXACRAD Final Report		S. Molendi et al., ESA contract n° 4000121062/17/NL/LF, 2021
[RD14]	MWG5.2-TN-0002-i1.1		An updated sky background model for ATHENA spectral simulations
[RD15]			

Contents

1. Introduction

The LEM (Line Emission Mapper) mission proposal envisions a cryogenic microcalorimeter array optimized for the 0.2–2 keV energy band, based on the X-IFU heritage. The array will consist of 13,806 absorber pixels with a 290 µm pitch, in hexagonal arrangement, that for a 4 m focal length will cover a solid angle equal to 29.4 square degrees. The orbit for LEM is currently under study with the Sun-Earth Lagrange points L1 and L2 possible candidates.

For what concerns the non X-Ray background (NXB), the premises are very similar to the X-IFU case. The background estimates are performed using Monte Carlo simulations with the Geant4 software [RD1] and, as a consequence, minor modifications to the X-IFU simulations can give precious insights on the NXB level to be expected for the instrument.

Furthermore, it is possible to test the effect of changes to the instrument mass model (sensitivity analysis) and identify the configuration that optimizes the detector performances.

2. Simulation settings and normalization procedure

For the LEM simulations the geometry and settings are the same we used for Athena [RD11], including the same GCR spectra [RD3], which are valid both for L1 and L2 orbits. The normalization procedure and the analysis logic are the same explained in [RD11], even if with different definition of in-band and out-of-band events. The same pixels size and arrangement as for X-IFU is used, with the same CryoAC, and the only difference in the geometry is the absorbers thickness of 0.64 um Gold[1].

In this simulation the location of the T0 filter is at Z = 110 mm, on top of the Nb chimney, the distance Nb-detector is 9.5 mm, and the distance Kapton-detector is 2 mm.

3. Results

The total level of background expected for LEM is 0.0247 cts/cm^2/s/keV in the 0.2-10 keV band, from all GCRs.

The relevant numbers are shown in Table 1, while the residual spectrum is shown in Figure 1.

[1] For reference, X-IFU has 4.2 µm of Bismuth and to 1.7 µm of Gold, with 245 µm x 245 µm pixels, 4 µm gap

Table 1

		GCR protons	GCR Alpha	GCR electrons
The total number of particles simulated		>~1356721842	>~123354914	>~69305311
Simulation equivalent time (ks)		~12.5	~12	~24
In-band background (BG)	(cts)	814	287	308
	(cts/cm^2/s/keV)	0.01583 ± 0.0006	0.0058 ± 0.0003	0.0031 ± 0.0002
Primaries in-band background (BG)	(cts)	0	0	0
	(cts/cm^2/s/keV)	0	0	0
Flux on the detector	(cts)	81755	13133	16341
	(cts/cm^2/s/keV)	2.86 ± 0.01	0.48 ± 0.004	0.296 ± 0.002
In-band flux on the detector	(cts)	46574	4775	10565
	(cts/cm^2/s/keV)	0.906 ± 0.004	0.097 ± 0.001	0.106 ± 0.001
Primaries flux on the detector	(cts)	47180	3878	1073
	(cts/cm^2/s/keV)	1.65 ± 0.01	0.142 ± 0.004	0.0194 ± 0.002

*Figure SEQ Figure * ARABIC 1 – The LEM unrejected background level and spectra induced by all GCR particles species. On the left with 1 keV bins, on the right with 0.1 keV bins.*

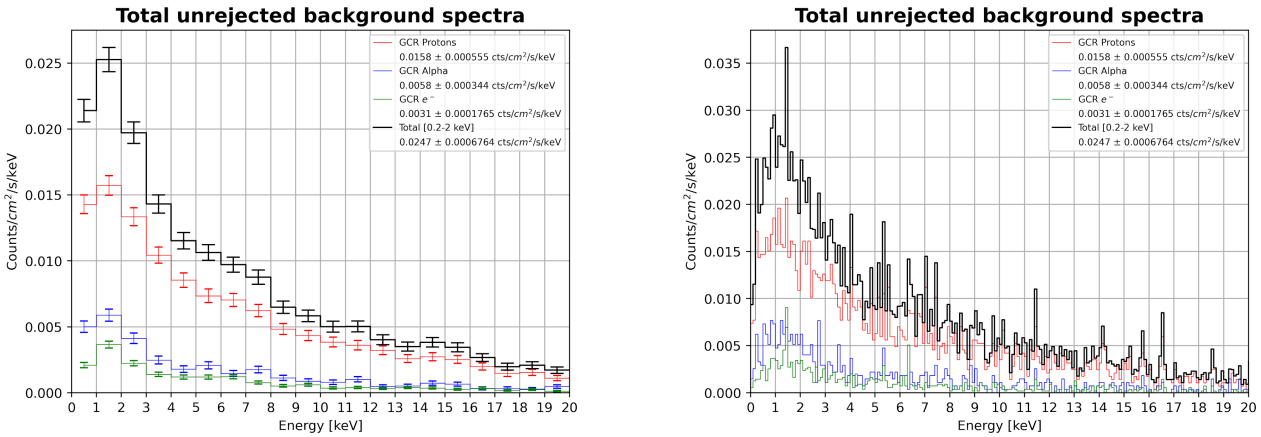

The unrejected background spectra show the signature of the Landau curve typical of the MIP (Minimum Ionizing Particles) energy depositions, and generally both the integrated level and the spectral shape are different than what is expected for X-IFU. The reason for this will be explored in section 4.

The initial energy spectra shown in Figure 2 show that roughly half of the particle flux impacting the detector is given by primary particles and the other half by secondaries. It is also clear that the low energy flux is dominated by secondaries, while due to the energy cut provided by the spacecraft and cryostat the primaries flux is negligible below 100 MeV.

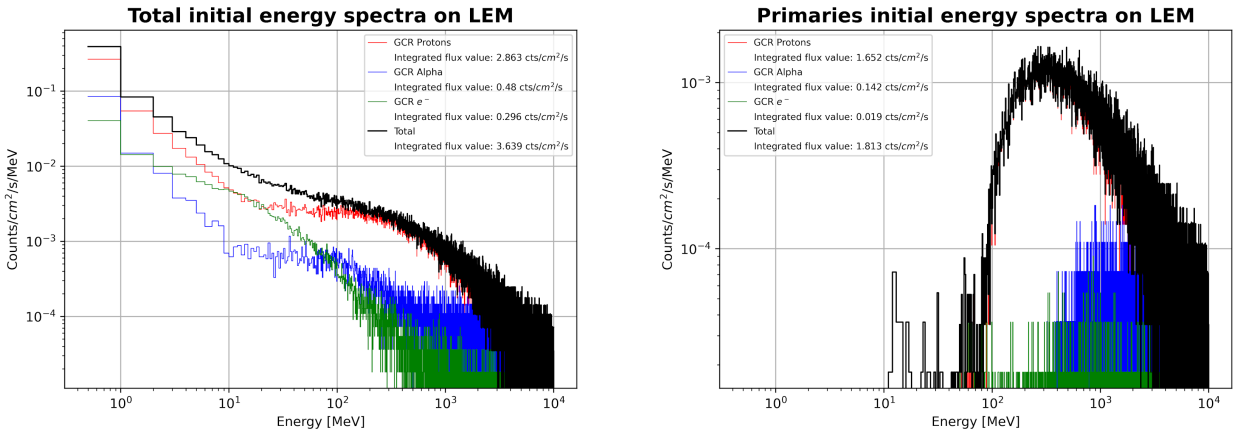

Figure 2 – The initial energy spectra of all the particles (left) and only the primaries (right) impacting the detector

The energy with which the particles hit the detector is show in Figure 3. The differences in the spectra among the different particles are probably due to the different initial spectra for the primaries and to secondary production rate that modifies the lower energy end of these spectra.

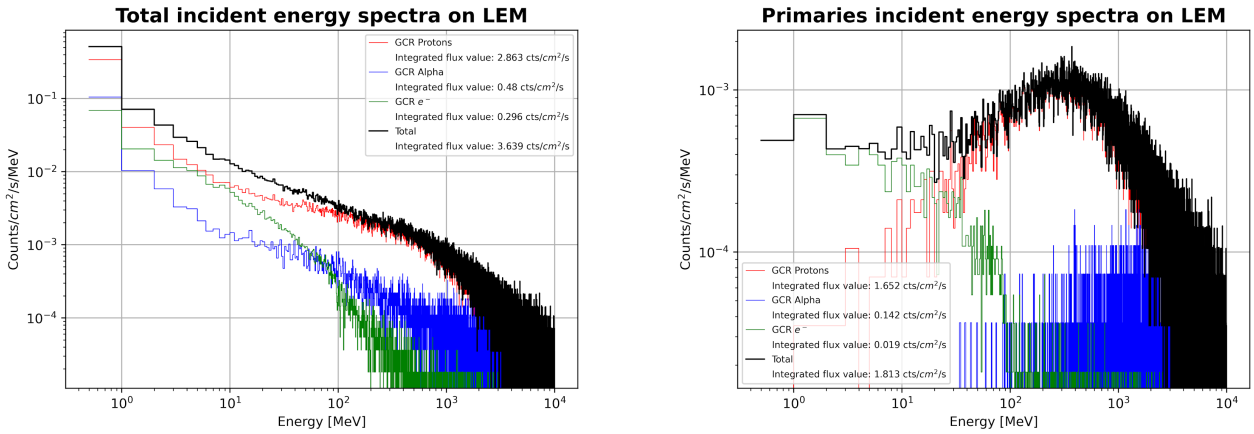

Figure 3 – The incident energy spectra of all the particles (left) and only the primaries (right) impacting the detector

3.1. Identified lines

The analysis software for Athena simulations has been adapted to LEM detectors' features. As an addition, a further analysis step that identifies lines and escape peaks in the simulations output has been created. The software checks the G4 fluorescence database and creates its own database of fluorescence lines and escape peaks. The software, in order:

1. Counts energy releases with the exact same energy
2. Searches for those energies in its internal fluorescence database
3. Searches for those energies in the escape peaks database

4. Removes from the possible escape peaks list all element pairs that do not contain the elements in the absorbers, and the ones that do contain elements not present in the geometry, generating a list of plausible elements pairs which can generate energy depositions of a given energy in the detector
5. Checks if any line has not been found and reports it. These not found energies could be
   5.1. The result of an escape peak photon from other 2 materials that impacts the detector, inducing a "second generation" escape peak
   5.2. Photons that randomly deposit very similar energies.

From a look at the original raw file with energy deposition from photons, given the low number of counts associated with these events, it seems like the second case is true for this dataset. The identified lines and escape peaks are plotted over the photons background spectrum in Figure 4 and listed in Table 2 and Table 3. In general, as it is for the X-IFU the detector is going to detect the fluorescence emission of every element it is in direct sight of.

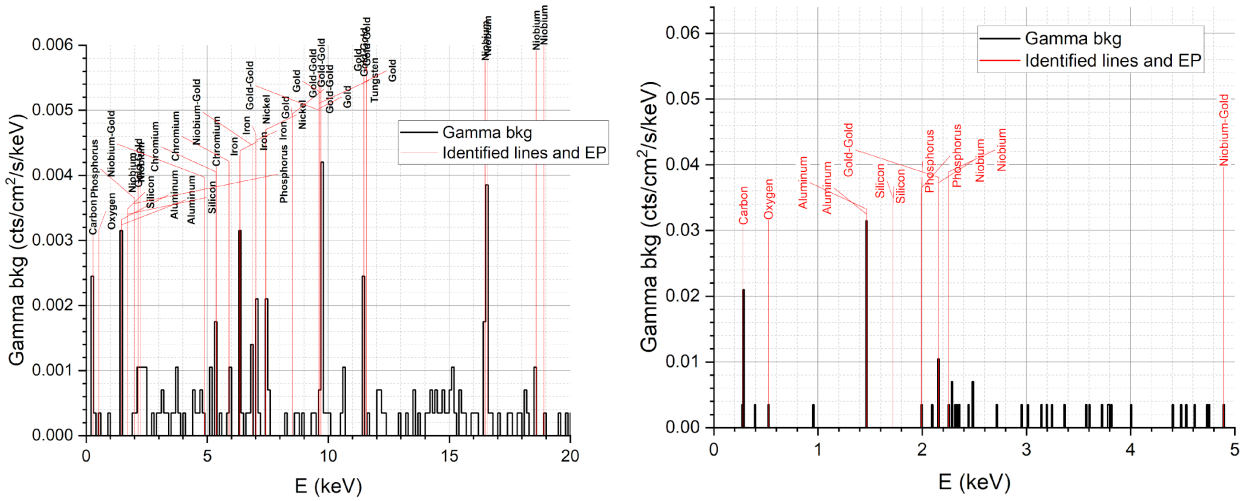

Figure 4 – the photons unrejected background spectrum, with the identified lines and escape peaks

Table 2 – Fluorescence line identified in the background, and the geometry volumes that contain the emitting element

E (keV)	Z	element	Volume
1.72052	14	Silicon	CryoAC , support Grid, wafer
1.71983	14	Silicon	CryoAC , support Grid, wafer
16.5789	41	Niobium	Niobium shield
9.7098	79	Gold	Absorbers, filters mesh, grid coating, passive shield, wafer coating, aperture cylinder coating
1.46917	13	Aluminum	Several FPA and cryostat elements
6.36271	26	Iron	Cryoperm, filters mesh, filters' supports
11.4753	79	Gold	Absorbers, filters mesh coating, grid coating, passive shield, wafer coating, aperture cylinder coating
1.4687	13	Aluminum	Several FPA and cryostat elements
6.34985	26	Iron	Cryoperm, filters mesh, filters' supports
5.37679	24	Chromium	filters mesh, filters' supports
0.28203	6	Carbon	MLI, filters mesh, filters' supports
1.99222	15	Phosphorus	filters mesh, filters' supports
5.36786	24	Chromium	filters mesh, filters' supports
7.43578	28	Nickel	Cryoperm, filters mesh, filters' supports
16.4814	41	Niobium	Niobium shield
18.5887	41	Niobium	Niobium shield
7.01695	26	Iron	Cryoperm, filters mesh, filters' supports
2.15729	41	Niobium	Niobium shield
11.5869	79	Gold	Absorbers, filters mesh, grid coating, passive shield, wafer coating, aperture cylinder coating
0.52309	8	Oxygen	MLI
8.5206	79	Gold	Absorbers, filters mesh, grid coating, passive shield, wafer coating, aperture cylinder coating
9.6213	79	Gold	Absorbers, filters mesh, grid coating, passive shield, wafer coating, aperture cylinder coating
9.6213	74	Tungsten	Not present escape peak
18.9096	41	Niobium	Niobium shield
1.99126	15	Phosphorus	filters mesh, filters' supports
2.25178	41	Niobium	Cryoperm, filters mesh, filters' supports
5.9074	24	Chromium	filters mesh, filters' supports
7.01536	26	Iron	Cryoperm, filters mesh, filters' supports
7.41782	28	Nickel	Cryoperm, filters mesh, filters' supports

Table 3 – plausible escape peaks among the identified lines

E (keV)	Escape Peak
9.7098	Gold-Gold
11.4753	Gold-Gold
6.8691	Niobium-Gold
2.15729	Gold-Gold
11.5869	Gold-Gold
4.8945	Niobium-Gold
8.5206	Gold-Gold
9.6213	Gold-Gold

4. Comparison with X-IFU

In Figure 5 it is shown the comparison among LEM and X-IFU background spectra in the 0.2-20 keV band. It is evident that the spectral shape and the integrated background levels are very different. Even if the 2 detectors work in different energy bands, the difference is not negligible and needs to be understood.

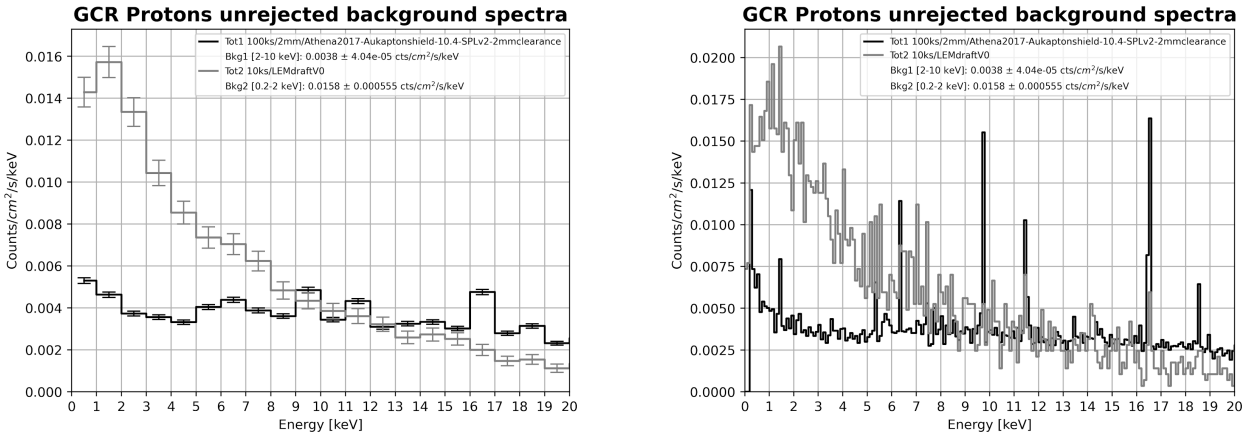

Figure 5 – comparison among LEM and X-IFU background spectra. On the left with 1 keV bins, on the right with 0.1 keV bins.

Looking at the comparison plots in Figure 6 we can confirm that incident particle fluxes that the X-IFU and LEM are identical as expected, so the difference must be in the particles' interaction with the sensor.

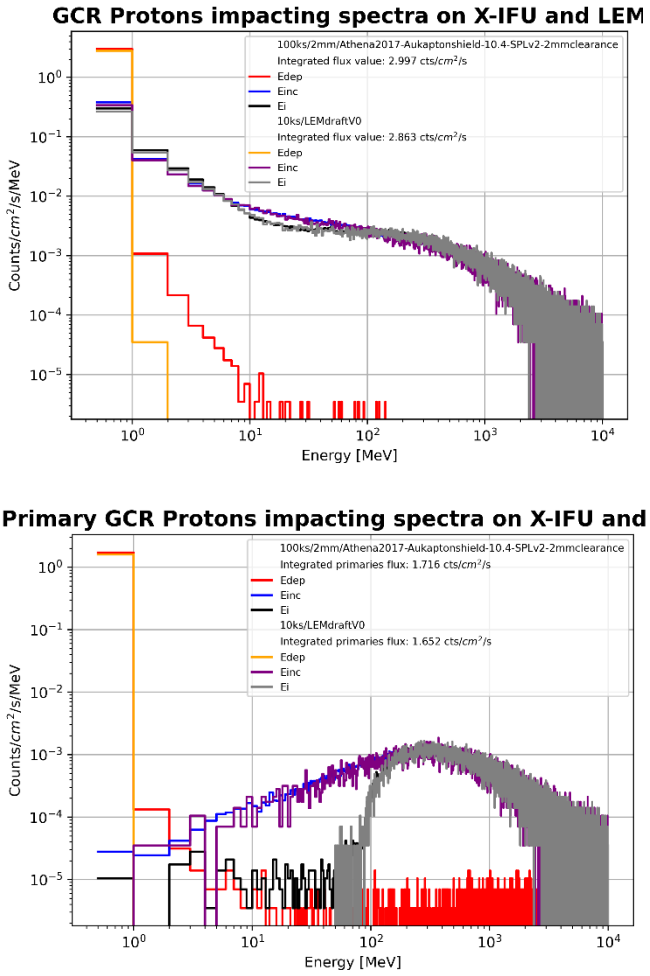

Figure 6 - comparison among LEM and X-IFU incident fluxes for all the particles (left) and only the primaries (right) impacting the detector

The reason for the background increment is evident if we look at the energy depositions on the detector from all the particles (from the GCR protons simulation only) and compare it to the X-IFU one (Figure 7) and the one induced by secondary electrons in LEM that represent 95% of the unrejected background (Figure 8, left) before CryoAC and pattern recognition.

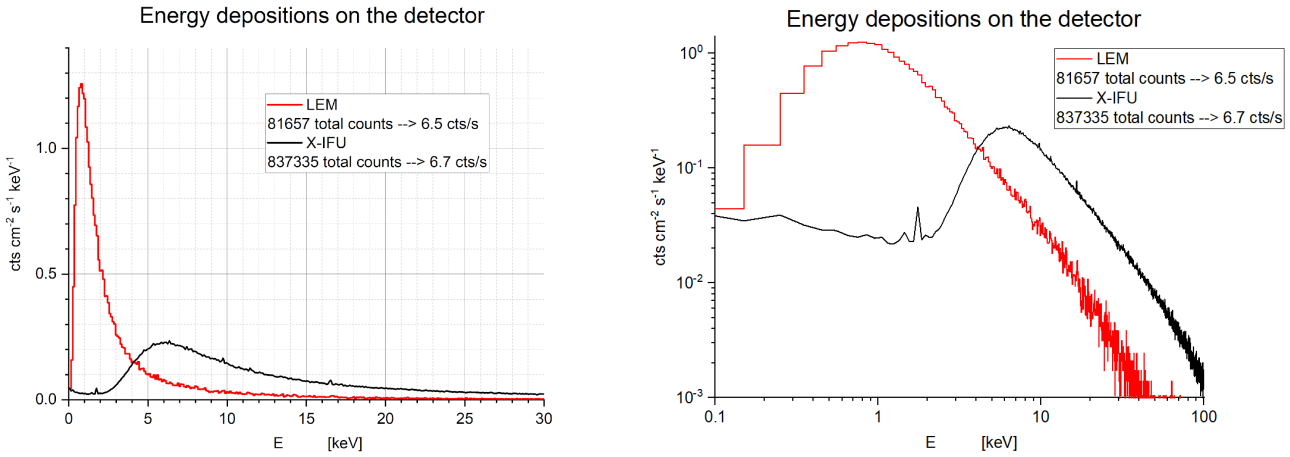

Figure 7 – energy depositions on the detectors

We can see that the MIP energy deposit has moved down to ~0.7 keV (as expected since the absorbers thickness is 1 order of magnitude lower), and it is now fully inside the sensitivity band of the instrument.

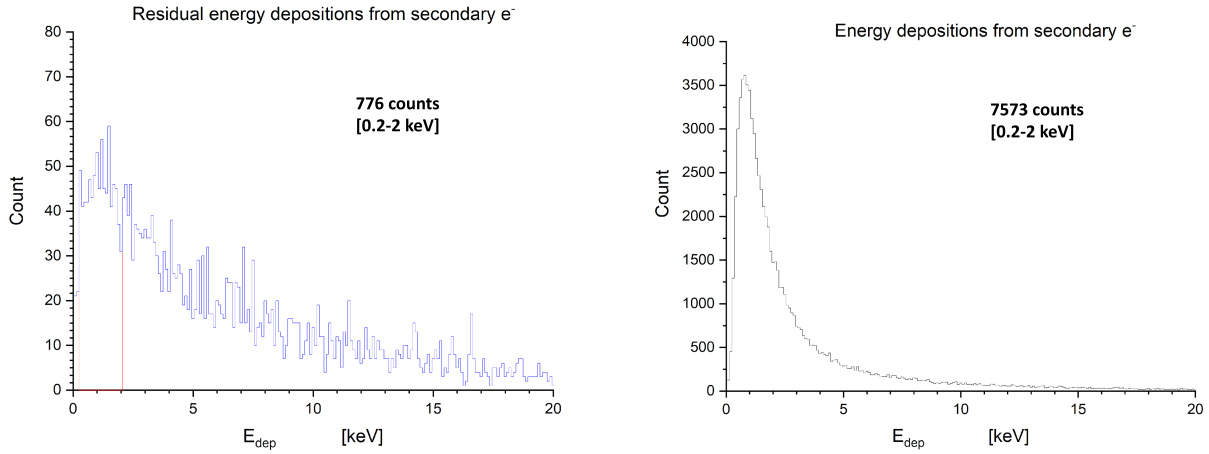

Figure 8 – On the left energy deposition of all secondary electrons impacting LEM, the peak position shows how most of them are in the MIP range. On the right energy deposition secondary electrons that induce unrejected background.

The LEM background has no contribution from MIP protons, despite their energy deposition being similar, meaning that the CryoAC is effectively vetoing most protons. Electrons however get deflected way easier after interacting with the main detector, which lowers the CryoAC effectiveness towards them with respect to the purely geometrical one.

If we look at the electrons' energy depositions after the CryoAC and pattern recognition (Figure 8, right), and compare it to the plot on the left, we can see that the CryoAC is still very effective at vetoing these events (~90% CryoAC efficiency for these particles), but their initial number increased by more than one order of magnitude with respect to the X-IFU case.

Finally, if we look at the distribution of incident energies of the electrons inducing background in the <2 keV band (Figure 9, left) we can see that (aside from the initial peak of fully absorbed particles) most of them have energies in the 100s keV, which is in the MIP range for electrons (Figure 9, right).

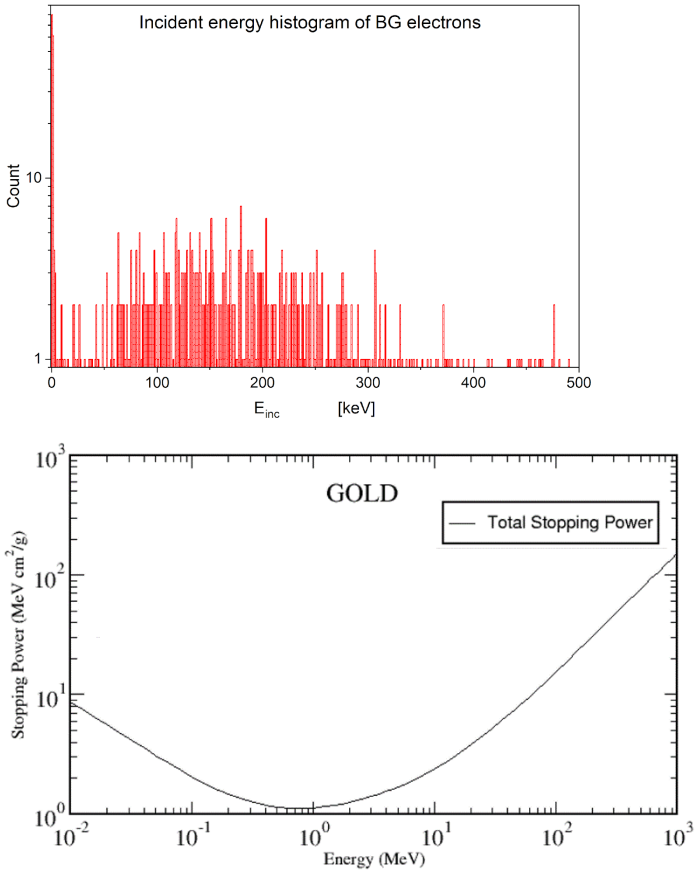

Figure 9 - Distribution of incident energies of the electrons inducing in-band background (left). Electrons stopping power for Gold (right) [RD12].

It is also likely that the backscattering contribution is reduced in the LEM detector and that these particles are geometrically missing the CryoAC, since we saw in EXACRAD that the maximum penetration depth for backscattered e^- in Au (90 keV, normal incidence) is 1.6 µm [RD13], so most of them will be able to cross the detector and exit on the other side in a completely random direction.

5. Comparison with CXB

We want to compare the level of unrejected background of 0.0247 cts/cm^2/s/keV, equivalent to 3.2×10^{-4} cts/arcmin^2/s/keV for the LEM telescope[2] (see Table 4), with the diffuse Cosmic X-ray Background flux.

The flux of CXB at 1 keV is 3×10^{-7} photons/cm^2/arcmin^2/s/keV [RD14], that with the 1600 cm^2 LEM effective area translates into 4.8×10^{-4} cts/ arcmin^2/s/keV on the detector. In conclusion we can expect an NXB level slightly lower than the CXB flux with the current detector and a X-IFU-like CryoAC.

[2] For a 4 m focal length 1 cm^2 = 76.86 arcmin^2

*Table SEQ Table * ARABIC 4 – LEM and X-IFU relevant numbers (before redefinition)*

If no CryoAC is foresaw (Figure 10), the expected in-band flux level is of 1.11 cts/cm^2/s/keV, equivalent to 1.44×10^{-2} cts/arcmin^2/s/keV, 30 times higher than the CXB level.

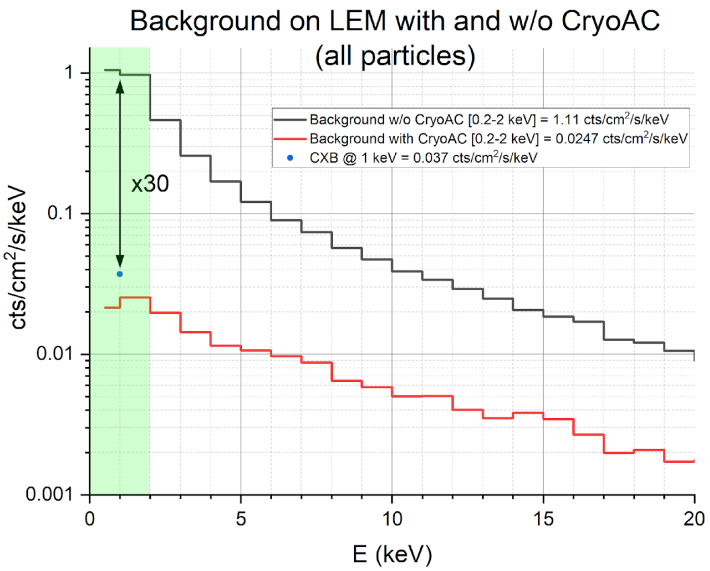

Figure 10 – The residual background with and without the CryoAC (red and black lines, respectively), and the CXB level at 1 keV for comparison

6. Final considerations

The presence of a X-IFU-like anticoincidence detector is mandatory to assure the NXB to be at least at the CXB level, otherwise CXB will be negligible with respect to the particle background. This is an unexpected result, and as it is explained in section 4, it is mainly due to the reduced thickness of the absorbers, that had the effect of concentrating the energy depositions from MIPs in the <2 keV energy band.

Even better would be the addition of a lateral anticoincidence such as the one we envisioned for X-IFU some time ago (Figure 11), to intercept the electrons scattered by the main detector (effectiveness to be quantified).

Alternatively, 2-3 times thicker absorbers could move the MIP deposition peak outside the energy band of the detector, reducing the in-band contribution, with an impact on the energy resolution to be quantified.

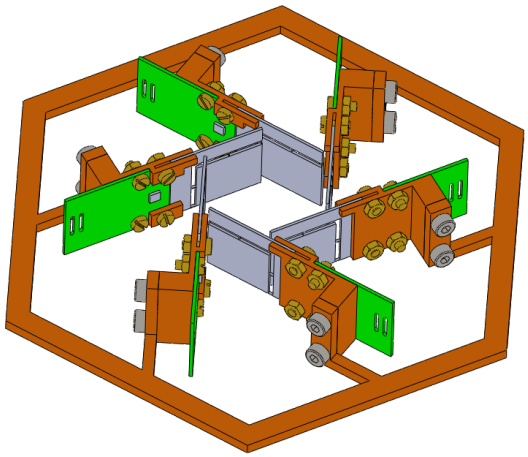

Figure 11 – first sketch of a lateral anticoincidence detector for X-IFU